Comparison Analysis of Bio-Inspired Tendon-Driven Manipulators Based on Their Tension-Feasible Workspace

Nicolas J S Testard, Christine Chevallereau, Philippe Wenger

Comparison analysis of bio-inspired tendon-driven manipulators based on their tension-feasible workspace

Nicolas J.S. Testard*
Nantes Université, Ecole Centrale de Nantes,
CNRS, LS2N, 44000 Nantes, France
Email: nicolas.testard@ls2n.fr

Christine Chevallereau
Nantes Université, Ecole Centrale de Nantes,
CNRS, LS2N, 44000 Nantes, France
Email: christine.chevallereau@ls2n.fr

Philippe Wenger
Nantes Université, Ecole Centrale de Nantes,
CNRS, LS2N, 44000 Nantes, France
Email: philippe.wenger@ls2n.fr

Bio-inspiration can be used in the development of novel dextrous and energy-efficient manipulators. This paper focuses on planar manipulators inspired by the bird neck, built upon stacking a series of tensegrity X-joints. The manipulators are actuated with four tendons, have different numbers of modules, with or without offsets. The objective of this work is to study the influence of offsets, number of modules, geometry of the joints, configuration at rest of the manipulators, and actuation scheme on the size of the tension-feasible workspace (TFW). The spring constants of the X-joints are determined so that the configuration at rest features a desired end-effector (EE) pose with minimal stiffness to ensure stability. Our study demonstrates that increasing the number of modules results in a larger TFW, although the number of active tendons is fixed. We find that the TFW can be maximized with appropriate modification of the joint geometry. Additionally, we explore the influence of bio-inspired approaches on the manipulator configuration at rest and actuation scheme in relation to the TFW. In addition, we conduct an analysis of the EE pose stiffness, revealing that offsets decrease this stiffness, while an optimal number of modules exists to achieve maximum stiffness. We observed that increasing the width of the manipulator generally enhances stiffness, while the configuration at rest and the actuation has little effects. Furthermore, experiments were conducted to validate the methodologies.

1 INTRODUCTION

Building modular manipulators brings many benefits. The number of modules should be decided upon considering several criteria, such as the minimum number required to accomplish the task, the possibility of having redundancy for a larger workspace, the cost, or the weight. The bird neck can be a source of inspiration to build new, light, and efficient manipulators based on tensegrity modules arranged in series [1]. The tensegrity modules used in this paper have one degree of freedom (DoF) and are operated by tendons in parallel with springs. An antagonist actuation is chosen to allow modulation of the stiffness of the manipulator [2]. In this study, we are interested in planar manipulators made of several such modules arranged in series.

A large amount of research work has been devoted to bio-inspired continuous-bodied manipulators [3]. Examples of manipulators inspired by animals are elephant-trunk arms [4, 5, 6], octopus' manipulators [7], snake-like manipulators [8], anguilliform manipulators [9].

Among these manipulators, continuum manipulators have been extensively developed. Detailed overviews of their design can be found in [10, 11]. These overviews present various types of continuum manipulators, including concentric tube manipulators, rod-driven continuum manipulators, fluid muscle robots, soft growing robots, and tendon-driven continuum manipulators. Models of these manipulators are discussed in [12, 13], with spe-

cific emphasis on tendon-driven manipulators in [14]. It is notable that while our manipulator is also tendon-driven, it stands apart due to its composition of non-flexible joints. Hence, its model, similar to the one obtained with the finite-dimensional approximation methods outlined in [12], can be established without approximation.

Observation of musculoskeletal systems, such as the bird neck or the human spine, suggests that increasing the number of modules can lead to improved performance. One of the objectives of this study is to examine whether this hypothesis holds true for the modular manipulators under investigation. A further aim of this research is to investigate the effect of bio-inspired configuration at rest and actuation scheme on this performance as well.

An essential metric for quantifying manipulator performance is the workspace size. [15, 16] have used it to compare tendon-driven continuum manipulators, which incorporate an elastic backbone, across various tendon routing configurations with or without payload. Additionally, [17] utilized this metric to compare tendon-driven manipulators with twin-pivot compliant joints, considering different tendon routing schemes and joint geometries. They examined how asymmetries in the joints can reshape the workspace. Tendons impose positive forces and these forces are limited by the actuators. The set of poses that satisfy the aforementioned constraints and in which the manipulator can balance a bounded set of external wrenches is called the wrench-feasible workspace (WFW) [18]. In the literature, the WFW is most often calculated for cable-driven parallel robots, see [18] and references herein. In our case, the system is subject to the forces of the springs and gravity, which must be compensated for by the tensions in the tendons. Excluding the consideration of additional external wrenches, we define the tension-feasible workspace (TFW) as the set of poses attainable with bounded actuation forces. Continuation methods have been employed to compute the WFW of a 2-DoF tensegrity manipulator [19]. The time taken for such computations has not been presented. A brute-force scanning technique was utilized in [20, 1], where a 2-dimensional (2D) scan was performed in the joint space of 2-degree-of-freedom (2-DoF) and 3-degree-of-freedom (3-DoF) manipulators to determine the TFW. The technique's limitation is that a high-resolution scan is necessary to acquire the boundary points with enough accuracy, which is impractical for manipulators with more than three modules. Interval analysis has been used to compute manipulator workspaces [21] of cable-driven parallel robots [18] with guaranteed results, but the high computational cost limits its practical implementation to manipulators with few DoFs.

This article extends the findings presented in [22]. It comprehensively revisits the impact of offsets and the number of modules on the TFW by adjusting the joint range conditions and considering a broader range of manipulators with varying numbers of joints and different offsets. This analysis elucidates how increasing the number of joints enhances the size of the TFW. Three new studies are introduced. The first investigates the effect of the ratio L/b and confirms the existence of an optimal value for maximizing workspace. It also confirms that adding offsets has minimal impact on the size of the TFW. The other two new studies explore the effects of the configuration at rest and tendon routing, respectively. This study on the influence of the number of modules, their geometry, the configuration at rest, and the routing of the tendons on the TFW for tendon-driven tensegrity manipulators has not been conducted before to the best of the authors' knowledge. Additionally, a study on the end-effector (EE) stiffness of the different manipulators is conducted with experiments, similar to the work of [23] for a manipulator with 2 modules.

The rest of this paper is organized as follows. The manipulators under study are described in section 2. The calculation of the TFW is discussed in section 3. Section 4 compares different 4-tendon, fully actuated or underactuated manipulators on the basis of their TFW. Section 5 presents some experimental results on the TFW and on the stiffness. The last section concludes the paper.

2 MANIPULATORS STUDIED

The manipulators studied in this paper are planar manipulators with 4 tendons and n identical modules ($n \geq 3$) arranged in a series. When $n > 3$, the manipulators are kinematically redundant since 3 DoFs would be enough to control the EE motion in the plane. Note that the tendons can only pull. Therefore, there should be at least one more tendon than the number of modules to control all the modules. Thus, $n > 3$ means that the manipulators are also underactuated [24].

2.1 Tensegrity modules

We want to define a planar tensegrity manipulator inspired by the bird neck by stacking several basic mechanisms or *modules*. These modules play the role of intervertebral joints. Each module consists of articulated bars and springs and is operated by cables. Springs and cables play the role of muscles and tendons. Tendon forces must be positive and are bounded by the maximum forces that the actuators can produce. Since only planar motions are involved, the relative motion between two ver-

tebrae is mainly a rotation. Both revolute joints and anti-parallelogram joints (referred to as X-joint) can be used to produce planar motions between two vertebrae, which can correspond to either a pure rotation or a translation coupled with a rotation [25]. The former generates a pure rotation about a fixed point, while the latter has a variable center of rotation. An important feature of the X-joint is its ability to increase stiffness under an increase in the antagonistic tendon forces, contrary to the revolute joint [26, 27]. Thus, we decide to use X-joints (Fig. 1, left). The ratio between the length L of the crossed bar and the length b of the base or top bar influences the kinetostatic performance of the X-joint. However, the choice of this ratio should also take into account the maximum and minimum elongation of the springs [20]. Different numbers of modules, with or without offsets, will be considered in this work. Figure 1 (right) shows a manipulator built with two X-joints and offsets..

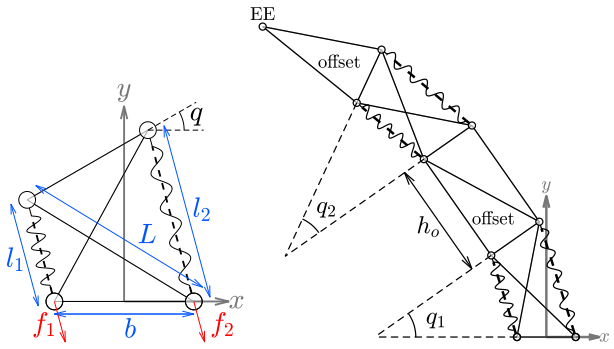

Fig. 1. X-joint tensegrity module (left) and manipulator made of two X-joints and offsets (right). The dashed lines correspond to the tendons in parallel with the springs. The solid lines correspond to rigid bars that are articulated at pivots represented by circles. The upper bar orientation with respect to the orientation of the lower bar is defined by angle q_i. The motion of the upper bar also includes a translational motion since the rotation is about the intersection of the diagonal bars and is not fixed.

2.2 Stack of modules

The manipulators at hand are composed of a stack of modules. The stack can be built with or without offsets. Offsets can be viewed as the possibility to adjust the dimensions of the vertebrae, or equivalently, the maximum reach of the manipulator, independently of the X-joints ratio L/b.

Let's define the joint configuration of the manipulator by $\mathbf{q} = [q_1, q_2, ..., q_n]^\top$, where q_i is the orientation angle between the base and top bar of each module, and n is the number of modules. Let $\mathbf{X} = [x_n, y_n, \gamma_n]^\top$ define the pose of the EE, i.e. the coordinates of the center of the top bar of the last module n and its orientation angle. We have:

$$\begin{cases} x_n = -\sum_{i=1}^{n} \sin(\gamma_{i-1} + \frac{q_i}{2})\sqrt{L^2 - b^2\cos^2(\frac{q_i}{2})} \\ \quad\quad -\sum_{i=1}^{n} \sin(\gamma_i) h_o \\ y_n = \sum_{i=1}^{n} \cos(\gamma_{i-1} + \frac{q_i}{2})\sqrt{L^2 - b^2\cos^2(\frac{q_i}{2})} \\ \quad\quad -\sum_{i=1}^{n} \cos(\gamma_i) h_o \\ \gamma_n = \gamma_0 + \sum_{i=1}^{n} q_i \end{cases} \tag{1}$$

where h_o is the offset height (Fig. 1, right), γ_i is the orientation angle of the i^{th} module with γ_0 being the orientation angle of the base bar.

2.3 Tendon routing

For a planar manipulator, three DoFs are sufficient to control its EE pose. We use n_f=4 tendons with remote motors on the base, regardless of the number of modules, in order to reduce inertia, complexity and costs. The minimum number of tendons required to effectively control 3 DoFs is 4. We operate our manipulator with a long tendon connected to all the modules on the right side and 3 shorter tendons grouping together sub-groups of modules (see Fig. 2, left). This choice results from a simplified implementation of the muscle organization of the bird neck with a long ventral muscle [1, 28]. However other actuation schemes will be studied in Section 4.4. With 3 modules, the system is fully actuated, and these short tendons actuate each of the modules independently, like in the prototype analyzed in [29] and in Section 5.

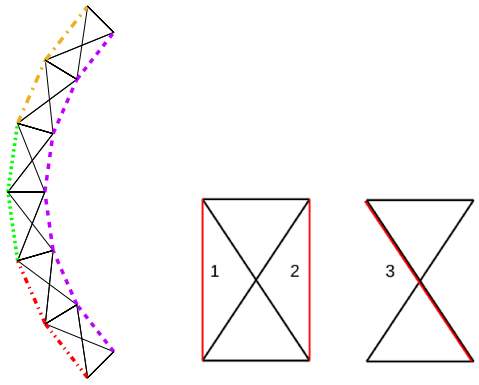

Fig. 2. Example of tendon routing with 6 modules: one long tendon on the right and three shorter tendons on the left (left). Tendon routing situations (center and right).

Each tendon can be routed in three different ways on each of the modules (see Fig. 2, center and right):

- tendon j placed on the left or right of module i, along the spring (Fig. 2, center): when this tendon is pulled, the associated motor changes the module orientation to reduce the tendon length on that side;
- tendon j runs along the bars of module i (Fig. 2, right): this routing allows to reach the modules above module i while eliminating the effect of the tendon on that module.

We define an actuation matrix $\mathbf{A}$ of size $(n \times n_f)$ as follows: each column j associated with tendon j describes how that tendon passes along module i. Each entry $A(i,j)$ can have three possible values 1 if the tendon passes to the left, 2 if the tendon passes to the right, 3 if the tendon j does not act on module i.

The unwound length of tendon j is denoted by l_j. Tendon length l_j can be expressed as follows [29]:

$$l_j = l_j^c + \sum_{i=1}^{n} l_j^{A(i,j)}(q_i) \tag{2}$$

where l_j^c is a constant. $l_j^{A(i,j)}$ depends on the tendon routing:

$$\begin{cases} l_j^1 = \sqrt{L^2 - b^2\cos^2(\frac{q_i}{2})} - b\sin(\frac{q_i}{2}) \\ l_j^2 = \sqrt{L^2 - b^2\cos^2(\frac{q_i}{2})} + b\sin(\frac{q_i}{2}) \\ l_j^3 = 0 \end{cases} \tag{3}$$

3 TENSION-FEASIBLE WORKSPACE

3.1 Static model

The static model is of primary importance for the study of tensegrity manipulators. It allows the determination of the manipulator configuration as a function of the tendon forces. The potential energy U of the manipulator can be written as

$$U = U_g + U_k + \sum_{i=1}^{4} f_j l_j, \tag{4}$$

where U_g (resp. U_k) is the contribution of gravity (resp. of all springs), l_j are the tendon lengths and f_j are the tendon forces. Each term $f_j l_j$ accounts for the potential energy associated with the tendon forces. The equilibrium condition of the manipulator is:

$$\frac{\mathrm{d}U}{\mathrm{d}\mathbf{q}} = 0 \tag{5}$$

Let $\mathbf{G} = \frac{\mathrm{d}U_g}{\mathrm{d}\mathbf{q}} + \frac{\mathrm{d}U_k}{\mathrm{d}\mathbf{q}}$ and $\mathbf{Z}(\mathbf{q}) = -\frac{\mathrm{dl}}{\mathrm{d}\mathbf{q}}$, where $\mathbf{l} = [l_1, l_2, l_3, l_4]^T$ and $\mathbf{f} = [f_1, f_2, f_3, f_4]^T$. The above equation can be written as:

$$\mathbf{G}(\mathbf{q}) = \mathbf{Z}(\mathbf{q})\mathbf{f} \tag{6}$$

The associated linearized model is written:

$$\left(\frac{\mathrm{d}\mathbf{G}(\mathbf{q})}{\mathrm{d}\mathbf{q}} - \frac{\mathrm{d}\mathbf{Z}(\mathbf{q})\mathbf{f}}{\mathrm{d}\mathbf{q}}\right)\delta\mathbf{q} = \mathbf{Z}(\mathbf{q})\delta\mathbf{f} \tag{7}$$

An equilibrium is stable if its stiffness matrix is definite positive:

$$\mathbf{K} = \frac{\mathrm{d}^2 U}{\mathrm{d}\mathbf{q}^2} > 0 \tag{8}$$

3.2 TFW calculation

3.2.1 *Joint space scanning*

A simple approach to calculate the TFW is to scan the joint space as suggested in [1]. The model (6) is solved to determine a force vector $\mathbf{f}$. If the number of tendons n_f is greater than the number of modules n, there are infinitely many solutions and one can choose the solution with minimum norm such that $0 < f_j < f_{max}$. This method cannot be used in our case for two main reasons. First, the computational cost increases exponentially with the number of modules, and second, it does not work for underactuated manipulators (i.e. when $n > n_f$). In fact, for the latter, the static model allows solutions only if $rank([\mathbf{G}(\mathbf{q}), \mathbf{Z}(\mathbf{q})]) = rank(\mathbf{Z}(\mathbf{q}))$.

3.2.2 *Force space scanning*

Scanning the force space is more tractable, since we have only 4 forces, regardless of the number of modules. For each $\mathbf{f}$ it is then necessary to solve Eq. (6) to find the equilibrium configuration $\mathbf{q_e}$. We then calculate the EE coordinates using Eq. (1).

As observed in [2, 20], several equilibrium solutions $\mathbf{q_e}$ can be obtained under two conditions: (i) the X-joints can reach a configuration close to their flat singularities and (ii) the gravity effects are dominant. In our case, the

spring effects are very large to ensure the stability of the equilibrium at rest compared to gravity. Moreover, since we impose limited tendon forces, the X-joints always remain far from their flat singularities. We then assume that there is only one stable feasible solution to Eq. (6). For a given set of input forces $\mathbf{f}_e$, we search for the solution $\mathbf{q_e}$ that minimizes $||\mathbf{G}(\mathbf{q_e}) - \mathbf{Z}(\mathbf{q_e})\mathbf{f}_e||$, using a Newton-Raphson approach. Starting from a configuration $\mathbf{q_{ep}}$, this method consists in writing the linearized model (7) in the neighborhood of this configuration. We compute the variation that tends to nullify $||\mathbf{G}(\mathbf{q_e}) - \mathbf{Z}(\mathbf{q_e})\mathbf{f}_e||$. The joint solution is updated as follows:

$$\mathbf{q_e} = \mathbf{q_{ep}} - \left(\frac{\mathrm{d}\mathbf{G}(\mathbf{q_{ep}})}{\mathrm{d}\mathbf{q}} - \frac{\mathrm{d}\mathbf{Z}(\mathbf{q_{ep}})\mathbf{f_e}}{\mathrm{d}\mathbf{q}} \right)^{-1} (\mathbf{G}(\mathbf{q_{ep}}) - \mathbf{Z}(\mathbf{q_{ep}})\mathbf{f}_e) \tag{9}$$

The solution is updated until:

$$||\mathbf{G}(\mathbf{q_e}) - \mathbf{Z}(\mathbf{q_e})\mathbf{f}_e|| < \epsilon \tag{10}$$

where ϵ is a decision parameter, which we take here to be $\epsilon = 10^{-6}$. The matrix to be inverted in (9) is actually the stiffness matrix $\mathbf{K}$ defined in Eq. (8). Thus, convergence is usually guaranteed whenever the equilibrium configurations are stable. On the other hand, the springs are chosen such that the equilibrium configuration at rest is stable (see below). Thus, we verify that a stable equilibrium solution is found. Unstable configurations will be discarded. The convergence speed depends on the initial configuration $\mathbf{q_{ep}}$, which must be close to $\mathbf{q_e}$. We start scanning the force space at $\mathbf{f} = 0$, which is the stable equilibrium configuration at rest. Thereafter, We compute the equilibrium state $\mathbf{q}_e$ for the different $\mathbf{f}$ using one of two methods: iterating from a previous equilibrium $\mathbf{q}_e$, or starting from a gravity-free equilibrium where the system behaves almost linearly. The selection of the method depends on the convergence behavior of the algorithm for the different cases studied. The TFW is then constructed in 3D (x_n, y_n, γ_n) space after computing the EE pose associated with each equilibrium configuration.

The force and workspace sampling data used are as follows. The maximum forces are set to $f_{max} = 140$ N. Nature often relies on frugality. Accordingly, our goal is to move with minimum actuation forces, as it minimizes the work during the movement and the material stress in the components. Since we are interested in poses that can be reached with small forces, we choose a non-regular sampling to explore more values for small forces. The tested forces are $0, 1, 2, 3, 5, 7, 9, 12, 16, 20, 25, 30, 35, ...130, 135, 140$ for each tendon. To plot the TFW, we define a regular grid along the coordinates x_n, y_n and γ_n. The grid is built in a box defined by $\pm 1.1h$ along x_n and y_n and $\gamma_0 \pm n\pi$ along γ_n, where h is the manipulator height in its vertical straight configuration and γ_0 is the orientation of the base bar of the first module. A TFW cell is declared reachable as soon as a pose of the EE belongs to it.

3.3 Example: a manipulators with 6 modules

In this section, we describe the case of a 6-X manipulator without offsets (shown in Fig. 2, left) to provide some additional information. The modules are similar to those used in the prototypes studied in [29, 30], with bar lengths of $b = 0.05$ m and $L = 0.1$ m. The corresponding module height is $h_m = 0.0866$ m, with a total height in a straight vertical configuration of $h = 6h_m = 0.516$ m. The module mass is 0.214 kg, distributed along the module bars. For a module, 3/11 of the mass is in the top bar and 4/11 is in the diagonal bars.

An essential element for the dimensioning of our manipulators is the choice of springs. The springs make it possible to define the equilibrium configuration at rest. The stiffer the springs, the higher the forces required to move the manipulator and, for the same maximum forces, the more the TFW is reduced. On the other hand, the role of the springs is to ensure the stability of the manipulator. It is particularly important that the equilibrium configuration at rest be stable. This allows the manipulator to remain in this configuration under small perturbations and without any actuation. The springs are thus chosen on the basis of the following two requirements:

- impose a desired EE pose at rest for a given base bar orientation;
- ensure stability at rest. We impose a positive stiffness via the smallest eigenvalue of the stiffness matrix $\mathbf{K}$, which must be greater than a prescribed minimal value, chosen here as $K_m = 1$ Nm/rad.

We want to limit the spring stiffnesses while satisfying the above constraints. The difference in stiffness between the two opposite springs in a module will modify the equilibrium configuration at rest, while the average value of the springs will contribute to the X-joint stiffness.

We first determine the equilibrium configuration $\mathbf{q_e}$ that will allow us to achieve the desired EE positions x_n^d and y_n^d and orientation γ_n^d while minimizing the norm of the joint configuration vector:

$$\begin{aligned} \mathbf{q_e} &= min_q ||\mathbf{q}|| \\ &s.t.\ [x_n(\mathbf{q}), y_n(\mathbf{q}), \gamma_n(\mathbf{q})]^\top = [x_n^d, y_n^d, \gamma_n^d]^\top \end{aligned} \tag{11}$$

We then calculate the spring constants as follows:

$$[\mathbf{k}_l^\top, \mathbf{k}_r^\top]^\top = min||\mathbf{k}_l + \mathbf{k}_r|| \quad s.t. \begin{cases} \mathbf{G}(\mathbf{q_e}) = \mathbf{0} \\ min(eig(\mathbf{K}(\mathbf{q_e}))) \geq K_m \end{cases} \tag{12}$$

where $\mathbf{k}_l$ (resp. $\mathbf{k}_r$) is a vector containing the spring constants on the left (resp. right) side of the manipulator.

In the example, the base of the first module of the manipulator has an initial orientation of $\pi/4$. The EE pose at rest is $x_n^d = 0$, $y_n^d = 0.9h$ and the orientation of the top bar is $\gamma_n^d = -\pi/4$. The spring constants are calculated to satisfy (12) for springs with a free length of $l_0 = L - b$. This value is chosen so that each spring is in tension for each orientation q_i of the module. The corresponding spring constants are $\mathbf{k}_l$=[2859, 2780, 2401, 1825, 1190, 676]$^\top$ Nm^{-1} and $\mathbf{k}_r$=[5258, 4692, 3851, 2832, 1813, 1027]$^\top$ Nm^{-1}. The resulting manipulator configuration at rest is shown in Fig. 2 (left).

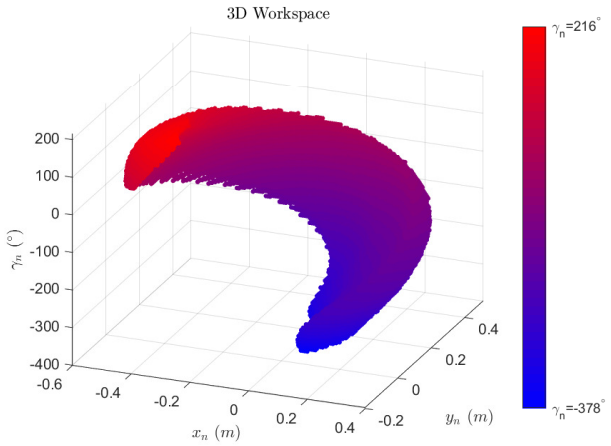

Fig. 3. TFW in (x_n, y_n, γ_n) for a 6-X manipulator. The orientation of the EE varies significantly with its position, but for a given pose the orientation range is limited.

Figure 3 shows the 3D TFW. Its shape looks like a twisted banana. This shows that the position and orientation coordinates are strongly coupled. Moreover, the banana is rather flat, which shows that the EE orientation range is limited at each position. Therefore, the manipulator is more suitable for positioning tasks. For now, the TFW will be analyzed mainly in terms of the point-reachable workspace, namely as the set of points associated with at least one feasible EE orientation [31]. Figure 4 shows the resulting 2D TFW. The TFW was calculated for the minimum forces: the orientation was then fixed by the minimum forces at each point. The colors indicate the maximum values of the force vector. The asymmetry in the workspace relative to the $x = 0$ axis is notable. This is due to the non-symmetric configuration at rest, which requires stiffer springs on the right side. The impact of the configuration at rest will be discussed in Section 4.3.

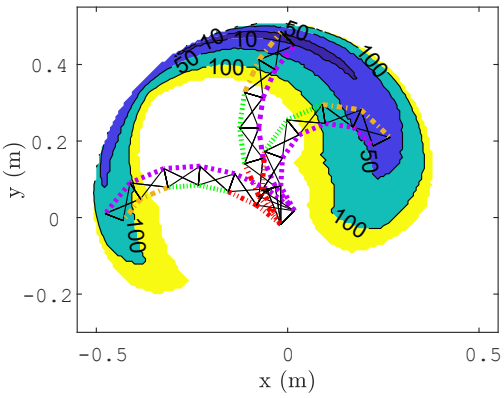

Fig. 4. TFW projected on (x_n, y_n). The minimum forces have been considered at each point and the colors indicate the maximum norm of the force vector (dark blue: $||\mathbf{f}||_\infty \leq 10$ N, blue: $10 < ||\mathbf{f}||_\infty \leq 50$ N, green: 50 N $< ||\mathbf{f}||_\infty \leq 100$ N, yellow: 100 N $< ||\mathbf{f}||_\infty \leq 140$ N). The manipulator shown in the middle is in its configuration at rest. At the EE poses $[-0.45, 0]^\top$ and $[0.24, 0.2]^\top$, the manipulator is shown with its EE orientation corresponding to minimal forces.

The purpose of this manipulator is to carry objects or exert forces in any direction while manipulating tools. The EE pose stiffness matrix can be expressed, with $\mathbf{J}_{xy} = \left[\frac{\partial x_n}{\partial \mathbf{q}}^\top, \frac{\partial y_n}{\partial \mathbf{q}}^\top\right]^\top$, by [32]:

$$\mathbf{K}_{xy} = \left(\mathbf{J}_{xy}\mathbf{K}^{-1}\mathbf{J}_{xy}^\top\right)^{-1} \tag{13}$$

To evaluate the ability of a manipulator to exert forces, this matrix can be analyzed. In a given EE position, the stiffness λ is such that $\lambda_m < \lambda < \lambda_M$, where λ_m (resp. λ_M) is the smallest (resp. highest) eigenvalue of $\mathbf{K}_{xy}$. Figure 5 (resp. 6) depicts the distribution of λ_m (resp. λ_M) in the TFW with minimal forces shown in Fig. 4. It is evident that for this manipulator, λ_m peaks in the right part of the TFW (which is the largest part), while λ_M is lowest in this region. Therefore, in this part of the TFW, the stiffness is the most uniform in any direction,

enabling the manipulator to exert similar forces in any direction for a given maximal EE deflection. It is noteworthy that, for a given pose, higher tendon tensions result in increased EE pose stiffness, in accordance with the properties of X-joints presented in Section 2.1. The following sections will focus primarily on the smallest eigenvalue, as it represents the minimum stiffness in any direction.

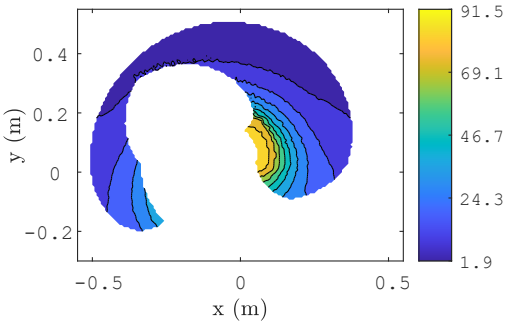

Fig. 5. Distribution of λ_m (in N/m) in the TFW in position with minimal forces

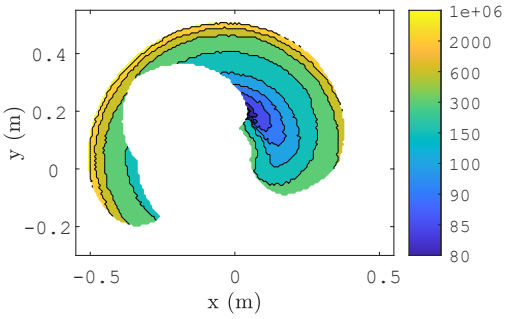

Fig. 6. Distribution of λ_M (in N/m) in the TFW in position with minimal forces.

4 TFW COMPARATIVE ANALYSIS

4.1 Influence of the offsets and number of modules.

The purpose of this section is to compare manipulators with different numbers of modules, with or without offsets. For more realistic comparisons, we impose similar features on all the manipulators studied:

- all modules in a given manipulator are identical with symmetric joint ranges $\pm\pi$;
- all manipulators have the same height h in their straight vertical configuration;
- all manipulators have the same width b;
- all manipulators have the same mass m_{tot}. We impose that each module has the same mass and that within a module, the mass is distributed between the offset and the rest of the joint proportionally to their height at $q_i = 0$.
- all manipulators have the same EE pose in their rest configuration;
- the stiffness in the rest configuration is greater than a given minimum value $K_m = 1$ N.m/rad to ensure stability.

A first objective is to study the effect of offsets and module height on the TFW size for fully actuated manipulators, i.e. with three modules. The bird neck contains a large number of vertebrae. However, it is not clear whether manipulators with a large number of modules would be the right choice, since the actuation system of our manipulators is a highly simplified implementation of the complex muscle organization of the bird neck. Therefore, a second objective is to study the effect of the number of modules on the size of the TFW.

4.1.1 *Manipulators compared*

For given module dimensions L and b, the module height in its zero orientation is $h_m = \sqrt{L^2 - b^2}$. We fix the height of all manipulators to be the same as in the example of Section 3.3, which is $h = 0.516$ m. If there is an offset of height h_o, the total height of a module becomes $h_1 = h_o + h_m$, while the total height of the manipulator remains fixed at $h = n.h_1$. This implies that h_m varies with h_o.

We consider several manipulators, each composed of $n = 3$ modules with offsets such that h_o/h_1 varies between 0 and 0.8. Additionally, we examine several offset-free manipulators with varying numbers of modules ranging from 3 to 42, ensuring that n is a multiple of 3. All manipulators are actuated with one long cable on the right and three cables on the other sides, pulling the same number of successive modules. In all cases tested, the configuration at rest is defined with the same EE pose and base bar orientation as the example in Section 3.3. The choice of these data allows the manipulators to feature a C-shape equilibrium configuration at rest. Although the rest configuration of the bird neck has a S-shape [28], this shape is difficult to achieve for manipulators with only 3 modules. In a C-shape configuration, the manipulator is not in a singularity and can therefore move more easily in all directions than in an I-shape configuration. Finally, to have a stable configuration, we impose a minimum stiffness at rest.

4.1.2 *Comparison results*

Figure 7 illustrates the TFW of several manipulators, including those without offsets and those with offsets. The TFW plots are arranged in a table with four rows and two columns. In the first column, all manipulators have 3 modules. The first (resp. second, third, fourth) has no offsets (resp. h_o/h_1 equal to $1/2$, $2/3$ and $3/4$). The manipulators in the second column have no offsets, the first (resp. second, third, fourth) has 3 (resp. 6, 9, 12) modules. Thus, in each of the four rows, the manipulators have the same module ratio L/b.

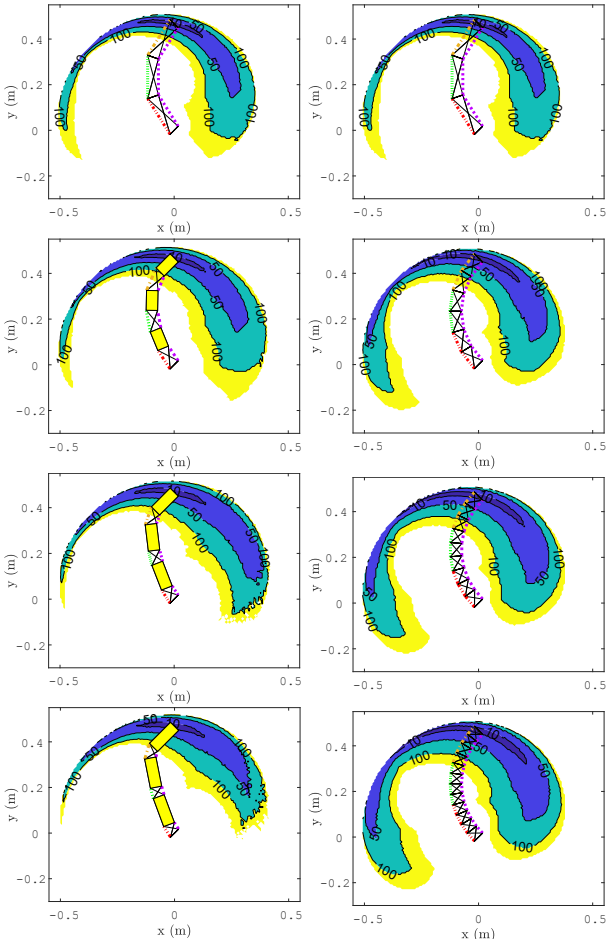

Fig. 7. Influence of the presence of offsets (first column) and of the number of modules (second column) on the TFW shape and size. The same TFW has been reproduced in the first row.

Figure 8 shows the TFW surface for several bounds on the forces. It is clear that the TFW surface increases with the value of f_{max}. For manipulators with 3 modules, the evolution of the TFW surface in function of the

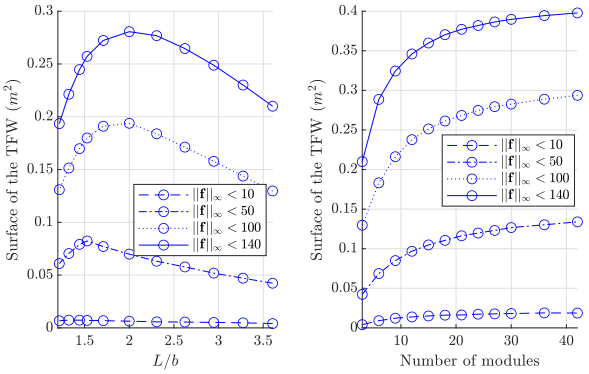

Fig. 8. Evolution of the TFW surface for manipulators with 3 modules as a function of the module ratio L/b (left) and for manipulators without offset as a function of the number of modules (right). Plots are provided for 4 maximum actuation forces.

offset height was not clear however looking at the evolution as function of the ratio L/b, it appears that larger TFWs are obtained when L/b equal to 2 for maximal tension of 100 and 140 N or equal or less of 1.5 for tension lesser than 50 N. It is interesting to note that this ratio of $L/b = 2$, is the one that provides the smallest ratio between minimum and maximum spring elongation, while providing the largest rotational range [20]. This study was conducted again with larger manipulators such that, without offset, the ratio L/b is equal to 2. It was observed that increasing the offset height directly diminished the TFW surface for maximum forces equal to or greater than 50 N. Therefore, the ratio L/b seems more significant for the TFW surface than the offset height. For manipulators with $n > 3$ modules, the TFW size increases with the number of modules. There is a significant increase in the TFW surface between 3 and 6 modules, after which the rate of increase diminishes with the number of modules. This can be explained by the fact that $L/b = 2$ for 6 modules. However, the observation that the TFW surface still increases with the number of modules, even when $L/b \neq 2$, suggests that having more modules is more influential for the TFW surface. However, it is not possible to increase the number of modules indefinitely, as the spring constants increase and the free lengths decrease, as represented in Table 1, leading to springs that are not technologically feasible.

For the different manipulators, the distribution of λ_m is similar to that depicted in Fig. 5, as shown by a selection of examples in Fig. 9. The stiffness peaks in the center of the right part of the TFW. However, the magnitude of this distribution varies between the manipulators. Figure 10 illustrates this variation by showing the maxi-

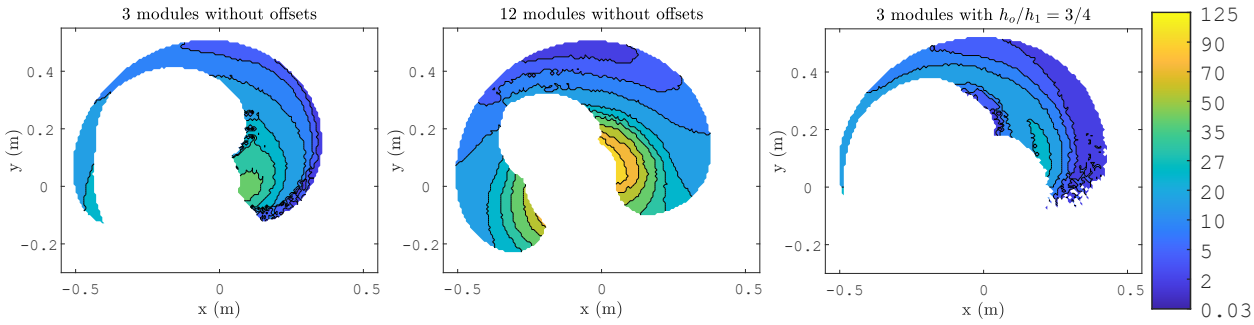

Fig. 9. Distribution of λ_m (in N/m) for the manipulator with 3 modules and no offset (left), the manipulator with 12 modules (center) and the manipulator with an offset $h_o/h_1 = 3/4$ (right). The stiffness increases with the number of modules and decreases with the offset height.

n	k_{max} (N/mm)	$k_{average}$ (N/mm)	l_0 (m)
3	3.8	2.1	$1.3.10^{-1}$
6	5.3	2.6	$5.0.10^{-2}$
12	7.9	3.8	$1.6.10^{-2}$
42	21.2	10.0	$1.5.10^{-3}$

Table 1. Evolution of the spring constants and free lengths with the number of modules. $k_{max} = max(k_l(i), k_r(i))$, $i = 1, ..., n$ and $k_{average} = mean(k_l(i), k_r(i)), i = 1, ..., n$.

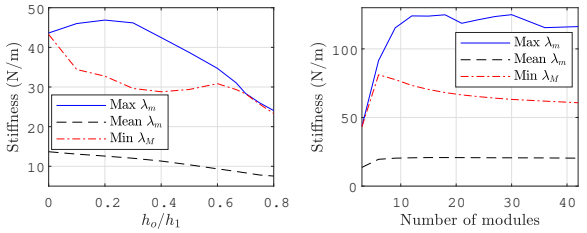

Fig. 10. Evolution of the maximum and mean λ_m and the minimum λ_M across the TFW for manipulators with 3 modules as a function of the offset height (left) and for manipulators without offset as a function of the number of modules (right).

mum and mean λ_m, and the minimum λ_M for all manipulators considered. The mean λ_M is not computed due to its tendency to approach infinity at singularities. Initially, both the maximum and mean λ_m and the minimum λ_M increase with the number of modules. However, after reaching 6 modules for the mean value and 12 modules for the maximum value, the increase stops. Conversely, the maximum λ_M decreases when the number of modules exceeds 6. Therefore, there appears to be an optimal range of 6 to 12 modules for achieving higher EE pose stiffness, particularly in the central right part of the TFW where λ_m is maximum and λ_M is minimum.

Regarding the influence of the offset height, these quantities generally decrease as the offset height increases.

4.2 Effect of the ratio L/b

To assess the impact of the L/b ratio, this section focuses on varying the width of the modules, b, while maintaining the same height in its zero orientation. First, this quantity will affect the contribution of the springs to the stability of the static equilibrium, since the lever arm of the spring action is directly affected by it. Similarly, the torque produced by the contribution of the actuation forces will increase or decrease with this quantity (the terms of $\mathbf{Z}$ are linear with respect to b for $q = 0$ [2]). Changing this parameter alone is not technologically realistic, since an increase in manipulator width must be accompanied by an increase in moving mass. We assume that the moving mass is well distributed along the planar manipulator, and therefore we adjust the weight of the manipulator proportionally to its width, keeping the same distribution assumptions along the bars (for a module, 3/11 of the mass in the top bar and 4/11 in the diagonal bars). We study the case of manipulators with 6 or 9 modules of constant height $h = 0.516$ m. The module width varies from $b = 0.01$ m to $b = 0.2$ m in both cases. The manipulators with $b = 0.05$ m are the same as in the previous section with the same mass. The springs are redefined for each design.

Figure 11 presents examples of some of the TFWs for different L/b ratios for manipulators with 6 modules and their corresponding stiffness distribution. Figure 12 shows the evolution of the TFW surface as a function of the ratio L/b for the manipulators with 6 and 9 modules. In each case it can be observed that there is a ratio value

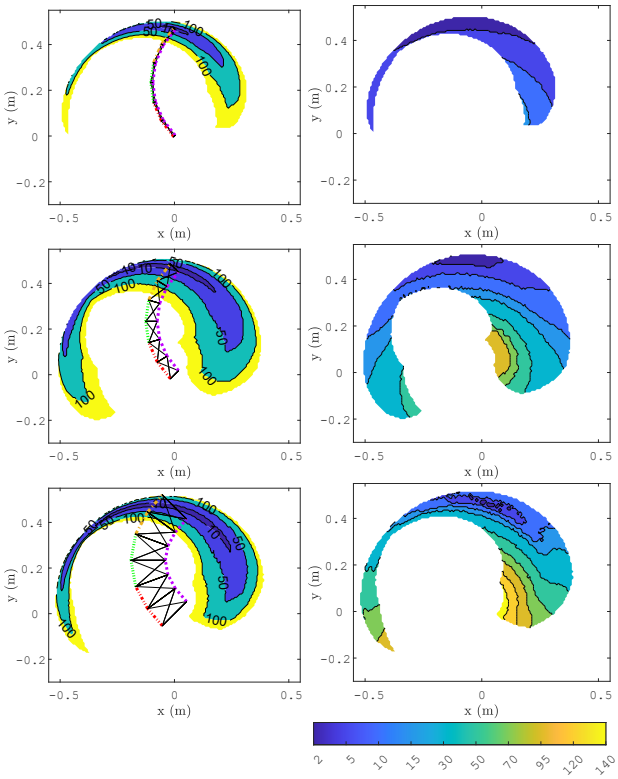

Fig. 11. Influence of the ratio L/b for a manipulator with 6 modules. From top to bottom, $b = 0.01$ m ($L/b = 8.7178$), $b = 0.05$ m ($L/b = 2$) and $b = 0.15$ m ($L/b = 1.1547$). The TFW are plotted on the left, and their corresponding distributions of λ_m are plotted on the right.

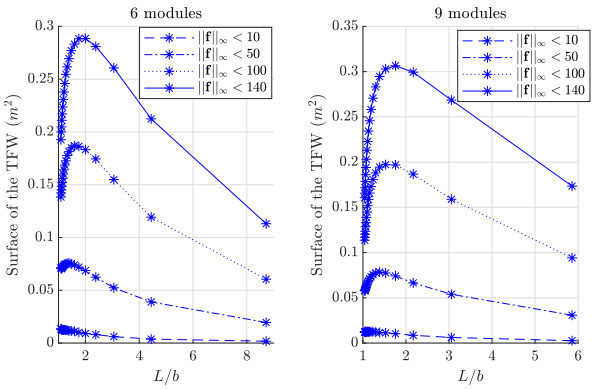

Fig. 12. Evolution of the TFW surface for manipulators with 6 modules (left) and 9 modules (right) as a function of the module ratio L/b. The height of the manipulator is fixed, the weight of the manipulator is proportional to its width.

that maximizes the TFW. This ratio evolves with the maximal forces in the tendons. For $f_{max} = 140$ we obtain a value of approximately 2 for 6 modules, whereas for 9 modules it is around 1.7.

Therefore, it can be concluded that the TFW can be influenced by the manipulator geometry. The optimal value for L/b varies with the number of modules and f_{max}.

For the EE pose stiffness, Fig. 11 shows a similar distribution of λ_m for different values of b, but with different amplitudes. The evolution of the maximum and mean λ_m and the minimum λ_M with respect to L/b for manipulators with 6 and 9 modules is shown in Fig. 13. It can be seen that in both cases the maximum and mean values of λ_m initially increase as L/b decreases, until this ratio approaches the geometric limit of 1, where it starts to decrease. This decrease starts around $L/b = 1.2$ for 6 modules and around $L/b = 1.1$ for 9 modules. The minimum λ_M, on the other hand, always increases as L/b decreases, tending to infinity as L/b approaches one. Thus, the stiffness of the EE pose generally increases as the ratio L/b decreases (i.e. as the width of the manipulator increases).

In the following, the value $L/b = 2$ will be retained because it is suitable in many cases to achieve a large TFW.

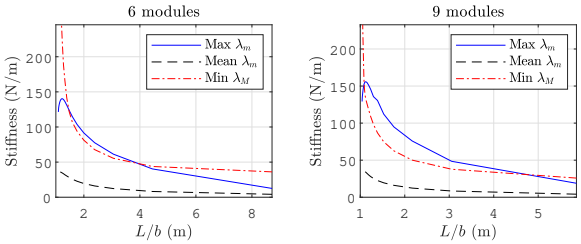

Fig. 13. Evolution of the maximum and mean λ_m and the minimum λ_M across the TFW as a function of L/b for manipulators with 6 modules (left) and 9 modules (right).

4.3 Choice of the configuration at rest

Based on the previous analysis, a manipulator with numerous modules and 4 tendons provides a large workspace. This architecture is also suitable for drawing inspiration from birds, as the number of vertebrae in their necks typically ranges from 9 to 26. Birds prefer a S-shape configuration at rest and an actuation scheme using a long ventral muscle. To justify the choice of the configuration at rest, we will compare three cases: straight neck (I-shape), C-shape, and S-shape with a long ventral muscle. We will consider three manipulators: 6 modules,

9 modules, and 12 modules.

We will consider modules with $b = 0.05$ m and $L/b = 2$. The mass and height h of each manipulator increase with the number of modules. The manipulator with 6 modules is the same as in Section 3.3. In each case, the I-shape features a straight, vertical configuration where all module angles are zero. In the C-shape configuration, the orientation of the base bar and the EE pose have the same constraints as in Section 3.3 with the EE pose varying along the y-axis depending on h. The S-shape configuration has the same constraints as the C-shape but with a base bar orientation of $-\pi/4$ instead of $\pi/4$.

The TFWs of the manipulator with 6 modules and their stiffness distribution are provided in Fig. 14. It can be observed that the general shape of the TFW is similar between the C-shape and S-shape configurations at rest, with a broader region on the right. The primary distinction between the TFWs of the C-shape and S-shape configurations is that the TFW of the S-shape exhibits a rightward shift compared to that of the C-shape. Additionally, the narrow portion of the TFW in the C-shape configuration is less noticeable in the S-shape configuration. On the other hand, the I-shape configuration exhibits a TFW that is relatively symmetric between the right and left, even though the actuation is not symmetric. The same findings for the TFW shape apply to the 9 and 12 modules. Regarding the EE pose stiffness distribution, it can be observed that the S-shape is similar to the C-shape, exhibiting higher stiffness in the right part of the TFW. The peak in the distribution of λ_m appears to cover a larger area in the C-shape configuration. In contrast, the I-shape configuration displays an almost symmetrical distribution, despite having asymmetric actuation. In the three considered cases, the amplitude of the maximum and mean λ_m appears similar, suggesting that it is independent of the configuration at rest.

Comparing the surfaces of the TFWs, as shown in Fig. 15, reveals some interesting results. In the case of 6 modules, the C-shape configuration stands out as the best for achieving the largest TFW. At lower forces ($||\mathbf{f}||\infty \leq 50$), the S-shape configuration comes second in terms of desirability, but with higher forces, the I-shape configuration yields a larger TFW than the S-shape configuration. However, for 9 and 12 modules, the I-shape configuration is less favorable. For 9 modules, the S-shape configuration is more appealing at lower forces ($||\mathbf{f}||\infty \leq 50$), but the TFW is larger for the C-shape configuration at higher forces. With 12 modules, the S-shape configuration provides the largest workspace for the considered tendon force amplitudes.

This suggests that the S-shape becomes increasingly

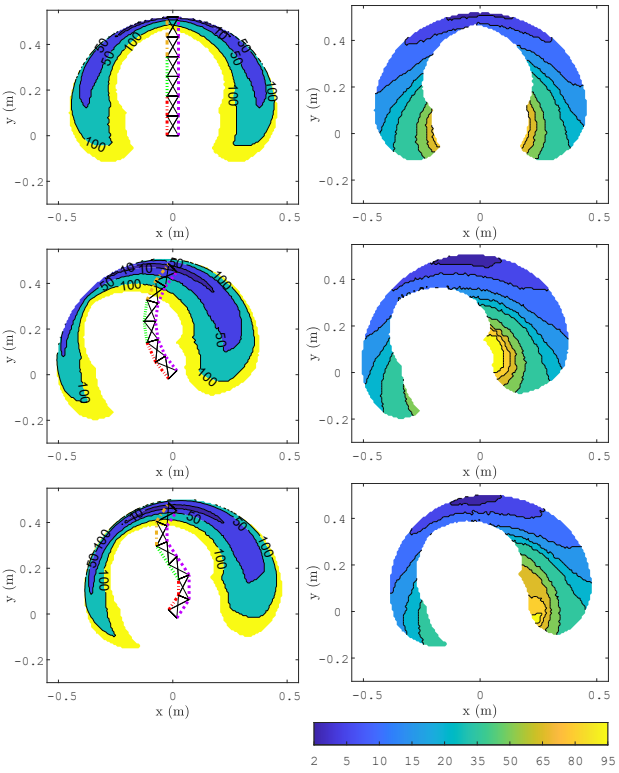

Fig. 14. Influence of the configuration at rest on the TFW for a manipulator with 6 modules (left) and their corresponding distributions of λ_m (right).

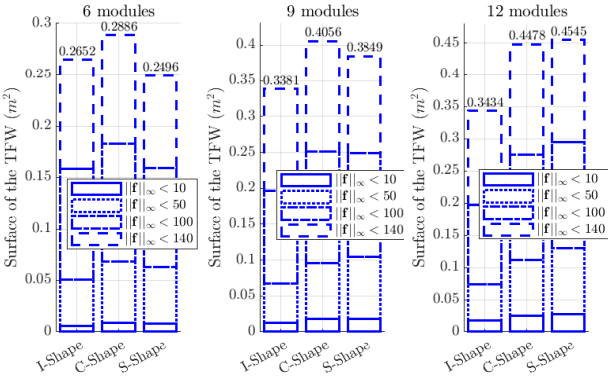

Fig. 15. TFW surface for manipulators with 6 modules (left), 9 modules (center), and 12 modules (right) depending on their configuration at rest (I-shape, C-shape or S-shape).

favorable as the number of modules increases. With 9 modules, the C-shape outperforms the S-shape only under high-force conditions. However, with 12 modules, it is noteworthy that when higher possible forces are imposed (e.g. 200 N), the C-shape offers a larger TFW than

the S-shape. Thus, to confirm that the S-shape configuration becomes more favorable with an increasing number of modules, the study was repeated with manipulators having the same mass as the 6-X manipulator. The results showed that the S-shape configuration becomes more favorable than the C-shape configuration starting from 21 modules for maximum forces of 140N.

In summary, the C-shape configuration at rest results in a larger TFW than the S-shape configuration when the maximum tendon forces are high enough. However, as the number of modules increases, the S-shape configuration becomes more advantageous for a given set of forces.

4.4 Choice of the actuation scheme

In the previous sections, we used an actuation scheme with one long tendon on one side and an even distribution of other tendons on the other side. This actuation scheme is not only inspired by the long ventral muscles of birds but also provides better velocity manipulability in some parts of the workspace than designs without long tendons [33]. In this section, we study the influence of the actuation scheme on the workspace.

The number of possible actuation schemes increases with the number of modules. Therefore, we will first focus on the manipulator with 6 modules of Section 3.3. As demonstrated in Section 4.3, the most suitable configuration at rest for this manipulator is the C-shape, which will be used for the study here. For this manipulator, we will initially study very different actuation schemes, including three cases where there is a long tendon on one side and three cases where there are two tendons symmetrically distributed on each side, such that there are two distinct groups of modules actuated by the same tendons.

We designate the various types of actuation by naming each tendon with L (left) or R (right) based on the side they pull the modules, with the module numbers they actuate as indices (e.g. the manipulator with 6 modules studied in Fig 2 (left) is $R_{123456}L_{12}L_{34}L_{56}$).

The TFWs of the manipulators with the studied actuation schemes are depicted in Fig. 16. Figure 17 presents the different TFW surfaces and volumes by considering the orientation of the EE as a third dimension.

One initial observation is that for the actuation with two tendons on each side evenly distributed ($R_{123}R_{456}L_{123}L_{456}$), the TFW is slightly larger than for the actuation with one tendon on one side and even tendon distribution on the other side ($R_{123456}L_{12}L_{34}L_{56}$), notably along the y-axis around the equilibrium configuration at $x = 0$. However, as shown in Fig. 17, we obtain a volume 2.5 times smaller for $R_{123}R_{456}L_{123}L_{456}$ than for $R_{123456}L_{12}L_{34}L_{56}$. This means that for a given position, the range of possible orientations is much smaller for $R_{123}R_{456}L_{123}L_{456}$. Therefore, these actuation schemes studied with two tendons on each side are less favorable if one wishes to modulate the EE orientation to some extent. A second observation is that for actuations with 2 tendons on each side, the TFW decreases as the tendon distribution becomes unequal.

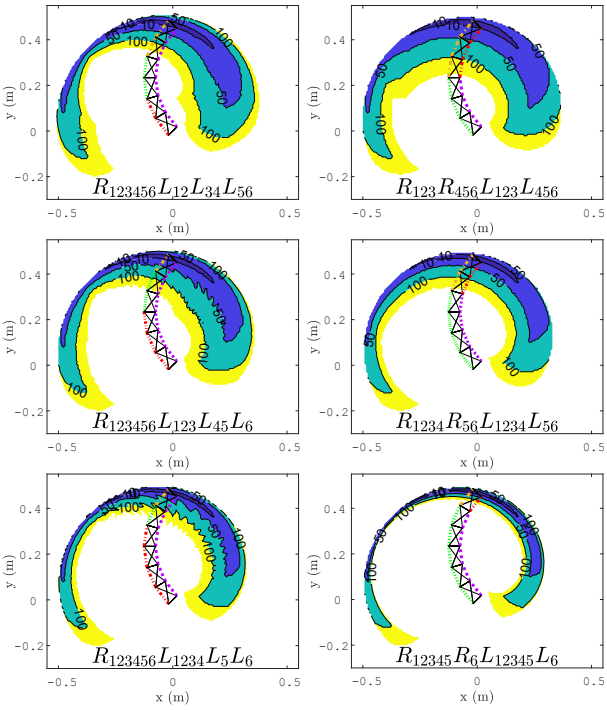

Fig. 16. Influence of the actuation on the TFW. First column, 1 long cable on the left and 3 more or less balanced groups on the right. Second column: actuation identical on the right and left with 2 groups of modules of more or less similar size.

For actuation schemes with one tendon pulling all the modules on one side, we observe that $R_{123456}L_{12}L_{34}L_{56}$ and $R_{123456}L_{123}L_{45}L_6$ have similar TFWs in terms of shape, surface, and volume. Thus, an even distribution of the tendons is not the only interesting case. This can be analyzed through bio-inspiration, [28,34] indicate that the bird neck can be separated into 3 to 9 subgroups that do not necessarily have the same number of vertebrae. However, the TFW of $R_{123456}L_{1234}L_5L_6$ is smaller than those of the two previous ones. In this case, the distribution becomes too uneven to be advantageous.

The distribution of λ_m for the different manipulators has not been depicted in this context. However, it closely resembles the distribution shown in Fig. 5. Unlike the manipulators studied in Sections 4.1 and 4.2, the amplitudes remain consistent across all manipulators. There-

fore, the actuation minimally impacts the EE pose stiffness.

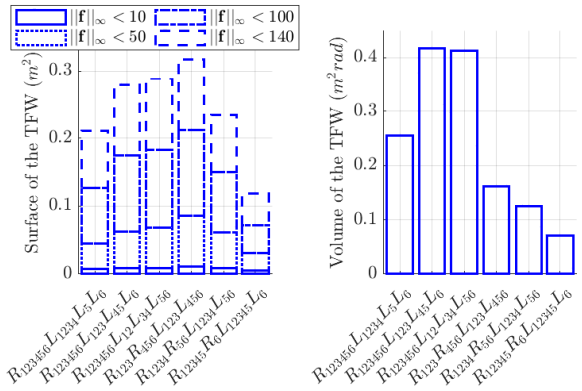

Fig. 17. TFW surface for 6-X C-shape manipulators with different actuation schemes (left). TFW volume for manipulators with different actuation for a maximum force of 140 N (right). Comparison between actuation schemes with one long tendon on one side and actuation with two tendons and each side

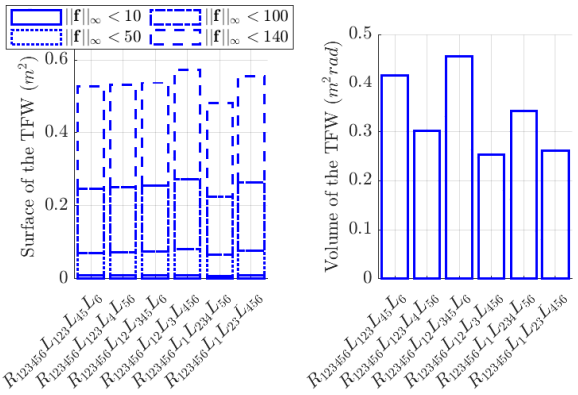

Fig. 18. TFW surface for 6-X C-shape manipulators with different actuation schemes (left). TFW volume for manipulators with different actuation for a maximal force of 140 N (right). Comparison between actuation schemes with one long tendon on one side and tendons that pull groups of 3, 2 and 1 modules on the other side.

We now study more actuation schemes with a long ventral tendon and 3 dorsal tendons pulling 3, 2, and 1 modules distributed in different ways similar to $R_{123456}L_{123}L_{45}L_6$. The results in terms of surface and volume are presented in Fig. 18. It can be observed that all these actuation schemes have fairly similar TFW surfaces. However, when we consider the volumes, we can see that $R_{123456}L_{123}L_{45}L_6$ and $R_{123456}L_{12}L_{345}L_6$ are better. Thus, the actuation with evenly distributed tendons or those with a group of one joint near the head are the most promising among the ones studied. Many other actuation schemes can be considered, notably those with tendons linked to non-successive joints, such as $R_{123456}L_{14}L_{25}L_{36}$. However, this specific configuration demonstrates a less favorable TFW, akin to that of $R_{12345}R_6L_{12345}L_6$; consequently, we omit the study of such cable routing between non-successive joints.

The study can also be extended to the 9-X S-shape manipulator discussed in Section 4.3.

We studied manipulators with a long tendon on one side and tendons pulling 4, 3, or 2 modules on the other side, as well as evenly distributed tendons. We found that configurations such as $R_{123456789}L_{1234}L_{567}L_{89}$, $R_{123456789}L_{123}L_{4567}L_{89}$ and $R_{123456789}L_{123}L_{456}L_{789}$ provide the largest TFW surface and volume. Thus, similar to the results on the 6-X manipulator, actuation with unevenly distributed tendons is most effective when the smallest module group is located near the head, as well as with evenly distributed tendons.

We now explore an intermediate actuation scheme for the 9-X S-shape manipulator that employs 2 tendons on each side, such that there are 3 distinct groups of 3 modules ($R_{123456}R_{789}L_{123}L_{456789}$ and $R_{123}R_{456789}L_{123456}L_{789}$). These actuation schemes are compared to the manipulator with a single long tendon on one side and evenly distributed tendons on the other ($R_{123456789}L_{123}L_{456}L_{789}$), as well as the manipulator featuring 2 tendons on each side, forming 2 groups of 5 and 4 modules ($R_{12345}R_{6789}L_{12345}L_{6789}$). The TFWs of these manipulators are shown in Fig. 19, and the comparison of their TFW surface and volume is presented in Fig. 20.

In each scenario, we observe that manipulators equipped with 2 tendons on each side exhibit a TFW with a larger area as compared to $R_{123456789}L_{123}L_{456}L_{789}$, particularly along the y-axis near the equilibrium configuration at rest. This result is similar to the 6-X C-shape manipulator.

Similarly to our previous investigation on the 6-X manipulator, $R_{12345}R_{6789}L_{12345}L_{6789}$ demonstrates a significantly smaller volume when compared to $R_{123456789}L_{123}L_{456}L_{789}$. However, $R_{123456}R_{789}L_{123}L_{456789}$ and $R_{123}R_{456789}L_{123456}L_{789}$ both exhibit substantial volumes, akin to that of $R_{123456789}L_{123}L_{456}L_{789}$. Therefore, these two new actuation schemes hold promise for achieving a large TFW. It can also be noted that while the volumes of $R_{123456}R_{789}L_{123}L_{456789}$ and $R_{123}R_{456789}L_{123456}L_{789}$ are greater than that of $R_{123456789}L_{123}L_{456}L_{789}$, it does

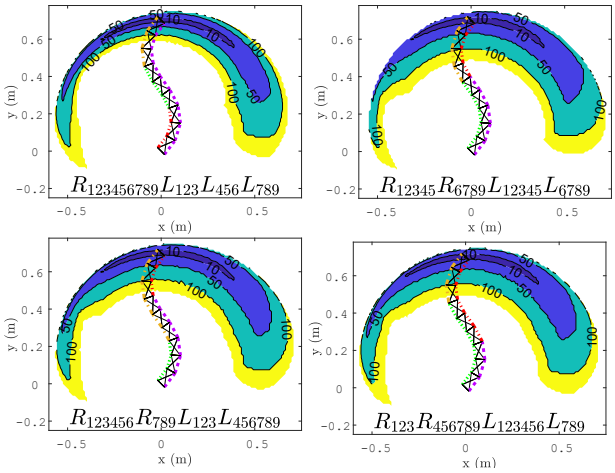

Fig. 19. TFW for 9-X S-shape manipulators with different actuation schemes. The first one is an actuation with one long tendon on one side and 3 tendons evenly distributed on the other side ($R_{123456789}L_{123}L_{456}L_{789}$). The second one is an actuation with 2 tendons on each side, resulting in 2 groups of 5 and 4 modules ($R_{12345}R_{6789}L_{12345}L_{6789}$). Third and fourth ones are 2 actuation schemes with 2 tendons on each side, creating 3 groups of 3 modules ($R_{123456}R_{789}L_{123}L_{456789}$ and $R_{123}R_{456789}L_{123456}L_{789}$).

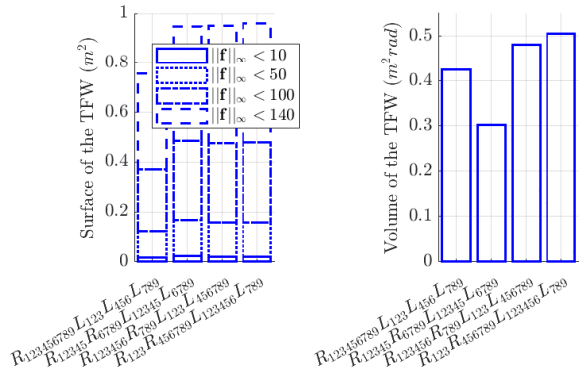

Fig. 20. TFW surface for 9-X S-shape manipulators with different actuation schemes (left). TFW volume for manipulators with different actuation schemes for a maximal force of 140 N (right).

not necessarily indicate a higher orientation range, as their surfaces are also larger.

5 EXPERIMENTAL RESULTS

In this section, we examine a prototype consisting of 3 modules without offset. One tendon pulls all the modules on the left, while three other tendons pull each module on the right. The prototype features $b = 0.05$ m and $L = 0.1$ m, with each module weighing 0.214 kg. The springs have identical stiffness values on the left and right parts of the joints, ranging from bottom to top at 600 N/m, 600 N/m, and 200 N/m, with a free length of 0.46 m. The orientation angle of the base bar $\gamma_0 = 0$ and the stable rest pose forms an I-shape. Encoders on the joints enable the computation of the joint angles $\mathbf{q}$. The prototype is shown in Fig. 21. Figure 22 gives a more detailed view of how one joint is constructed and how the tendons are attached.

The TFW of this manipulator is represented in Fig. 23, where the minimum force imposed is not 0 but 10 to ensure tendon tensions. The motors have a maximum torque limitation, which results in a maximum tendon tension of 90 N with the chosen drum and gear ratio. Therefore, the TFW has been computed for tensions ranging from 10 to 90 N with a step of 1 N. Due to the presence of dry friction in the prototype, obtaining the exact same joint angles $\mathbf{q}$ for a given force vector $\mathbf{f}$ is complicated, and obstacles also limit the reachable EE pose. However, two extreme poses attained by the prototype are represented in this figure, showing that the TFW drawn is likely correct.

For the stiffness experiment, the tendon tensions are set to 50 N in each tendon, resulting in an equilibrium pose of approximately $\mathbf{q} = [0°; 3.7°; -4.8°]^\top$ (which is not exactly null due to the influence of pulleys through which the tendons pass). A dynamometer is attached to the top right part of the manipulator and is pulled horizontally. The experimental setup is illustrated in Fig. 21.

The position $[x_r, y_r]^\top$ where the dynamometer is attached is defined by:

$$\begin{cases} x_r = x_n + \frac{b}{2}\cos\gamma_n \\ y_r = y_n + \frac{b}{2}\sin\gamma_n \end{cases} \tag{14}$$

The stiffness matrix of the point where the dynamometer is attached is given by $\mathbf{K}'_{xy} = \left(\mathbf{J}'_{xy}\mathbf{K}^{-1}\mathbf{J}'^{\top}_{xy}\right)^{-1}$ with $\mathbf{J}'_{xy} = \left[\frac{\partial x_r}{\partial \mathbf{q}}^\top, \frac{\partial y_r}{\partial \mathbf{q}}^\top\right]^\top$.

The numerical value of this matrix at the considered position and for the imposed tendon tensions is:

$$\mathbf{K}'_{xy} = \begin{bmatrix} 87 & 528 \\ 528 & 4181 \end{bmatrix} \tag{15}$$

The eigenvalues are $\lambda_m = 20$ N/m and $\lambda_M = 4248$ N/m associated with the eigenvectors $\mathbf{v}_m = [-0.9920, -0.1261]^\top$ and $\mathbf{v}_M = [0.1261, -0.9920]^\top$. As expected from the manipulator configuration, the stiffness is lowest near the horizontal axis.

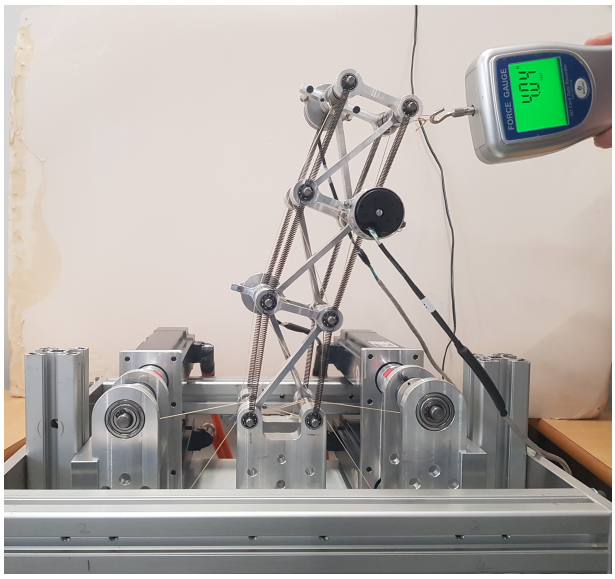

Fig. 21. Prototype with 3 modules. The tendons are pulled with a tension of 50 N.

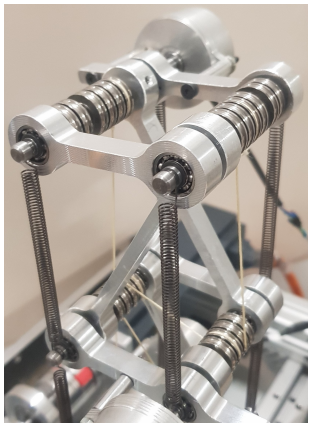

Fig. 22. Module of the prototype.

As depicted in Fig. 21, the manipulator is pulled with a force of 4.04 N, resulting in an approximate angle of $\mathbf{q} = [-17°, -3°, -3°]^\top$. Dividing the applied force by the horizontal displacement yields a stiffness of approximately 54 N/m. This value differs from the theoretical 20 N/m due to the applied large displacement and the friction. Nevertheless, the order of magnitude of this stiffness remains similar.

6 CONCLUSION

A family of planar manipulators built upon stacking a series of tensegrity X-joints has been analyzed in this paper. The manipulators are actuated with four tendons, regardless of the number of modules. The main goal of this work was to study the influence of offsets, number of modules, geometry of the joints, configuration at rest of the manipulators and actuation scheme on the TFW size. The manipulators spring constants were determined so that the configuration at rest features the desired EE pose with minimal stiffness to ensure stability.

We have shown that the more the number of modules, the larger the TFW. However, the increase in the number of modules is limited by the feasibility of the required springs. In this study, it is observed that the effect of offsets did not demonstrate a significant impact. In fact, the module ratio turned out to be of more importance for these manipulators. In particular, a ratio of L/b close to 2 appears to be the most suitable for achieving the largest TFW. It has been noted that the C-shape configuration at rest outperforms the S-shape one only when forces are substantial. However, as the number of modules increases, for a given set of forces, the S-shape configuration gradually surpasses the C-shape one in terms of TFW surface. Regarding actuation, using two tendons evenly and symmetrically distributed on each side resulted in a larger workspace in terms of position but a significantly limited orientation range. Conversely, actuation with a single tendon on one side, with tendons either evenly distributed or unevenly distributed on the other side and the smallest group of modules near the head, provides a large workspace with improved orientation modulation. An intermediate actuation scheme featuring two tendons on each side, resulting in three equally distributed groups of modules, was subsequently investigated. The results revealed that this compromise yields a better TFW while preserving the advantages of both previously explored actuation schemes.

The study into the stiffness of the EE pose revealed several key findings. We observed that: (i) there exists an optimal number of modules to achieve higher EE pose stiffness, (ii) the offset height tends to decrease the manipulator EE pose stiffness, (iii) the EE pose stiffness generally increases as the ratio L/b decreases, without approaching the geometric limit too closely (iv) both the actuation schemes and the configuration at rest have negligible effects on the minimum EE pose stiffness.

This paper serves as a preliminary investigation into the design of a tendon-driven tensegrity manipulator. Payloads can also be considered, as demonstrated in [35] for 2-DoF manipulators. The TFW was calculated upon scanning the force space. Another possibility could be to scan the workspace. This will be the object of future work. Furthermore, we will also study the impact of obstacles. Kinematically redundant and under-actuated ma-

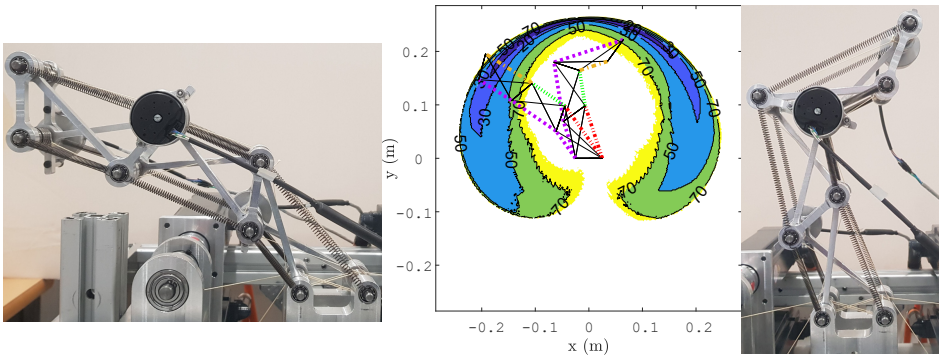

Fig. 23. TFW of the Prototype with 2 poses of the EE attained by the prototype. The represented limits on the maximum value of the force vector are 20, 30, 50, 70, and 90 N.

nipulators should have a better capability to adapt to cluttered environments by shaping around obstacles.

REFERENCES

[1] B. Fasquelle, M. Furet, P. Khanna, D. Chablat, C. Chevallereau, and P. Wenger, "A bio-inspired 3-dof light-weight manipulator with tensegrity x-joints," in *2020 IEEE Int. Conf. on Robotics and Automation*, pp. 5054–5060, IEEE, 2020.

[2] A. Van Riesen, M. Furet, C. Chevallereau, and P. Wenger, "Dynamic analysis and control of an antagonistically actuated tensegrity mechanism," in *ROMANSY 22–Robot Design, Dynamics and Control*, pp. 481–490, Springer, 2019.

[3] D. Trivedi, C. Rahn, W. Kier, and Y. Parker, "Soft robotics: Biological inspiration, state of the art, future research," *Applied Bionics and Biomech.*, pp. 99–117, 2008.

[4] M. Hannan and I. Walker, "Analysis and initial experiments for a novel elephant's trunk robot," in *Proceedings. 2000 IEEE/RSJ Int. Conf. on Intelligent Robots and Systems*, vol. 1, pp. 330–337 vol.1, 2000.

[5] Q. Guan, J. Sun, Y. Liu, N. M. Wereley, and J. Leng, "Novel bending and helical extensile/contractile pneumatic artificial muscles inspired by elephant trunk," *Soft Robotics*, vol. 7, no. 5, pp. 597–614, 2020. PMID: 32130078.

[6] Y. Liu, Z. Ge, S. Yang, I. D. Walker, and Z. Ju, "Elephant's Trunk Robot: An Extremely Versatile Under-Actuated Continuum Robot Driven by a Single Motor," *Journal of Mechanisms and Robotics*, vol. 11, 07 2019. 051008.

[7] C. Laschi, M. Cianchetti, B. Mazzolai, L. Margheri, M. Follador, and P. Dario, "Soft robot arm inspired by the octopus," *Advanced Robotics*, vol. 26, no. 7, pp. 709–727, 2012.

[8] R. Buckingham, "Snake arm robots," *Industrial Robot*, vol. 29, no. 3, pp. 242–245, 2002.

[9] M. Porez, F. Boyer, and A. J. Ijspeert, "Improved lighthill fish swimming model for bio-inspired robots: Modeling, computational aspects and experimental comparisons," *The International Journal of Robotics Research*, vol. 33, no. 10, pp. 1322–1341, 2014.

[10] J. Burgner-Kahrs, D. C. Rucker, and H. Choset, "Continuum robots for medical applications: A survey," *IEEE Transactions on Robotics*, vol. 31, pp. 1261–1280, Dec. 2015.

[11] M. Russo, S. M. H. Sadati, X. Dong, A. Mohammad, I. D. Walker, C. Bergeles, K. Xu, and D. A. Axinte, "Continuum robots: An overview," *Advanced Intelligent Systems*, vol. 5, no. 5, p. 2200367, 2023.

[12] C. Della Santina, C. Duriez, and D. Rus, "Model-based control of soft robots: A survey of the state of the art and open challenges," *IEEE Control Systems*, vol. 43, pp. 30–65, June 2023.

[13] C. Armanini, F. Boyer, A. T. Mathew, C. Duriez, and F. Renda, "Soft robots modeling: A structured overview," *IEEE Transactions on Robotics*, vol. 39, pp. 1728–1748, June 2023.

[14] P. Rao, Q. Peyron, S. Lilge, and J. Burgner-Kahrs, "How to model tendon-driven continuum robots and benchmark modelling performance," *Frontiers in Robotics and AI*, vol. 7, 2021.

[15] D. C. Rucker and R. J. Webster Iii, "Statics and dynamics of continuum robots with general tendon routing and external loading," *IEEE Transactions on Robotics*, vol. 27, pp. 1033–1044, Dec. 2011.

[16] J. Starke, E. Amanov, M. T. Chikhaoui, and

J. Burgner-Kahrs, "On the merits of helical tendon routing in continuum robots," in *2017 IEEE/RSJ International Conference on Intelligent Robots and Systems (IROS)*, (Vancouver, BC), pp. 6470–6476, IEEE, Sept. 2017.

[17] J. Barrientos-Diez, M. Russo, X. Dong, D. Axinte, and J. Kell, "Asymmetric continuum robots," *IEEE Robotics and Automation Letters*, vol. 8, pp. 1279–1286, Mar. 2023.

[18] M. Gouttefarde, D. Daney, and J.-P. Merlet, "Interval-analysis-based determination of the wrench-feasible workspace of parallel cable-driven robots," *IEEE Transactions on Robotics*, vol. 27, no. 1, pp. 1–13, 2011.

[19] Q. Boehler, I. Charpentier, M. Vedrines, and P. Renaud, "Definition and computation of tensegrity mechanism workspace," *Journal of Mechanisms and Robotics*, vol. 7, 2015.

[20] M. Furet and P. Wenger, "Kinetostatic analysis and actuation strategy of a planar tensegrity 2-x manipulator," *ASME J. of Mechanisms and Robotics*, vol. 11, no. 6, p. 060904, 2019.

[21] D. Chablat, P. Wenger, F. Majou, and J. P. Merlet, "An interval analysis based study for the design and the comparison of three-degrees-of-freedom parallel kinematic machines," *The International Journal of Robotics Research*, vol. 23, no. 6, pp. 615–624, 2004.

[22] N. J. S. Testard, C. Chevallereau, and P. Wenger, "Comparison Analysis of Tendon-Driven Manipulators Based on Their Wrench Feasible Workspace," in *Cable-Driven Parallel Robots* (S. Caro, A. Pott, and T. Bruckmann, eds.), Mechanisms and Machine Science, (Cham), pp. 121–133, Springer Nature Switzerland, 2023.

[23] M. Furet and P. Wenger, "Kinetostatic analysis and actuation strategy of a planar tensegrity 2-X manipulator," *Journal of Mechanisms and Robotics*, vol. 11, Dec. 2019.

[24] M. Carricato and J.-P. Merlet, "Stability analysis of underconstrained cable-driven parallel robots," *IEEE Transactions on Robotics*, vol. 29, no. 1, pp. 288–296, 2012.

[25] M. Furet, A. Abourachid, C. Bohmer, V. Chummunb, C. Chevallereau, R. Cornette, X. D. L. Bernardie, and P. Wenger, "Estimating motion between avian vertebrae by contact modeling of joint surfaces," *Computer Methods in Biomechanics and Biomedical Engineering*, 2021.

[26] V. Muralidharan and P. Wenger, "Optimal design and comparative study of two antagonistically actuated tensegrity joints," *Mechanisms and Machine Theory*, vol. 159, p. 104249, 2021.

[27] V. Muralidharan, N. Testard, C. Chevallereau, A. Abourachid, and P. Wenger, "Variable Stiffness and Antagonist Actuation for Cable-Driven Manipulators Inspired by the Bird Neck," *Journal of Mechanisms and Robotics*, vol. 15, no. 035002, 2023.

[28] L. Terray, O. Plateau, A. Abourachid, C. Böhmer, A. Delapré, X. de la Bernardie, and R. Cornette, "Modularity of the Neck in Birds (Aves)," *Evolutionary Biology*, vol. 47, pp. 97–110, June 2020.

[29] B. Fasquelle, P. Khanna, C. Chevallereau, D. Chablat, D. Creusot, S. Jolivet, P. Lemoine, and P. Wenger, "Identification and control of a 3-x cable-driven manipulator inspired from the bird neck," *ASME J. of Mechanisms and Robotics*, pp. 1–25, 2021.

[30] N. J. S. Testard, C. Chevallereau, and P. Wenger, "Dynamics and computed torque control stability of an under-actuated tendon-driven manipulator," in *Advances in Mechanism and Machine Science* (M. Okada, ed.), Mechanisms and Machine Science, (Cham), pp. 332–341, Springer Nature Switzerland, 2023.

[31] R. Vijaykumar, K. Waldron, and M. Tsai, "Geometric optimization of serial chain manipulator structures for working volume and dexterity," *The International Journal of Robotics Research*, vol. 5, no. 2, pp. 91–103, 1986.

[32] A. Albu-Schaffer, M. Fischer, G. Schreiber, F. Schoeppe, and G. Hirzinger, "Soft robotics: what cartesian stiffness can obtain with passively compliant, uncoupled joints?," in *2004 IEEE/RSJ International Conference on Intelligent Robots and Systems (IROS) (IEEE Cat. No.04CH37566)*, vol. 4, pp. 3295–3301, Sept. 2004.

[33] V. Muralidharan, P. Wenger, and C. Chevallereau, "Kinematic and Static Analysis of a Cable-Driven 2-X Tensegrity Manipulator for Two Actuation Strategies," in *Advances in Robot Kinematics 2022*, pp. 149–159, Springer International Publishing, 2022.

[34] R. D. Marek, P. L. Falkingham, R. B. J. Benson, J. D. Gardiner, T. W. Maddox, and K. T. Bates, "Evolutionary versatility of the avian neck," *Proceedings of the Royal Society B: Biological Sciences*, vol. 288, p. 20203150, Mar. 2021.

[35] V. Muralidharan, P. Wenger, and C. Chevallereau, "Design considerations and workspace computation of 2-x and 2-r planar cable-driven tensegrity-inspired manipulators," *Mechanism and Machine Theory*, vol. 195, p. 105610, 2024.